WILEY | Hindawi

Research Article

Experimental Study on Energy Dissipation of Saturated Mudstone in Coal Mine under Impact Loading

Liangjie Guo [1,2] and Yongyu Wang [1]

^{1}Faculty of Engineering, China University of Geosciences, Wuhan 430074, China
^{2}Engineering Research Center of Rock-Soil Drilling & Excavation and Protection, Ministry of Education, Wuhan 430074, China

Correspondence should be addressed to Yongyu Wang; yywang@cug.edu.cn

The influence of blasting energy on blasting fragmentation and damage of reserved rock is important for safety and schedule of drill-blasting construction in coal mine. This study is aimed at investigating the dynamic mechanical properties of mudstone in coal mine using the energy characterization method, and their quantitative relation formula was also developed. The impact compression experiments of mudstone in Huainan mining area were conducted to study the saturated mudstone dynamic mechanism, crack properties, and energy dissipation law using the diameter 50 mm split Hopkinson pressure bar (SHPB). The results show that under the back-and-forth reflection of the stress wave, the saturated mudstone specimens are characterized by circumferential failure and axial splitting damage, which appear in the rock grain interface. By energy analysis, the energy dissipation per volume (EDV), energy dissipation per mass (EDM), and absorption impedance energy ratio (AIER) are used to represent the energy dissipation characteristic of mudstone. And the AIER is the best index. Additionally, there is the quadratic function relationship between three indexes and average strain ratio, showing the dependence of the strain ratio.

1. Introduction

Mudstone is widely distributed in coal measure strata, which is characterized by loose, poor cementation and low strength. Hence, mudstone is extremely sensitive to stress, moisture, temperature, and subsurface water [1, 2]. The mechanical property and inner structure of mudstone vary with the change of stress condition [3–5]. Many researchers studied the physical and mechanical properties and failure laws of mudstone in coal mine under complex natural environment conditions. The strength of mudstone is less than 30 MPa, reviewing the existing literature researches. And its strength would be lower when faced with water, temperature, weathering, and so on [6, 7]. Bhattarai et al. investigated the effect of chemical and physical weathering on the shear strength of the mudstone [8]. The results showed that the shear strength of fully weathered mudstone is 10 times larger than that of weak weathered mudstone. Huang et al. carried out a series of uniaxial compression experiments

and creep experiments of mudstone specimens under different water contents and found that the rock strength and elastic modulus decreased rapidly with the increment of water content, and a nonlinear creep constitutive equation was established based on the experimental data [9]. Both Zhang et al. and Lu et al. studied the softening effect of mechanical properties of mudstone under high temperatures [10, 11]. High temperatures would cause thermal expansion of mudstone, and the expansion will increase with temperature increasing.

Due to the effects of impact loading, such as blasting and mechanical vibration in coal mine, the disturbance range of surrounding rock mass in roadway increases, yet the bearing capacity of rock mass decreases. Hence, the roof fall and rock bottom drum are easily happened [12–15]. The dynamic behavior of rock under impact loading is an important issue for coal mining [16, 17]. Some typical complete dynamic stress-strain curves for marble and granite using SHPB technique are given by Shan et al. [18], together with

an interpretative discussion on the shapes and meanings of the curves. Chen et al. tested the dynamic mechanical behavior of granite [19]. The results showed that impact dynamic strength increases as the precompression stress increases and can reach its maximum when the precompression stress is about 50% of the static tension strength. Liu et al. studied the mechanic properties of amphibolites, sericite-quartz schist, and sandstone under impact loading and analyzed the dynamic compressive strength, failure modes, and energy dissipation variation with the strain rate and the strain rate hardening effect from the perspective of sandstone microstructure [20]. Mardoukhi et al. used optical microscopy and profilometry to analyze the drop rate of tension strength and damage area of rock under impact loading using SHPB tests [21]. The dynamic mechanics of granitic specimens under different hydrostatic pressures were studied by Du et al., and the results showed that the dynamic strength of rock specimens increased with increasing the strain rate, while the rate sensitivity of rock strength decreased as the hydrostatic pressure increased [22]. The thermal effect on the dynamic properties of rock is another significant issue for deep coal mining. Fan et al. investigated the effects of high temperature on the dynamic behavior of granite using SEM and SHPB tests, and the results showed that both the dynamic strength and energy absorption capacity decreased as temperature increased [23].

Many researchers studied the failure morphology of rock specimens under impact loadings. And Chinese scientists have made tremendous achievements. Li et al. studied the impact failure characteristics of rock subjected to one-dimensional coupled static and dynamic loads [24]. Rock specimens will break with a shear failure model subjected to one-dimensional coupled static and dynamic loads, while the failure mode will be splitting faulting for conventional impact testing. Zhao et al. considered that the impact failure of rock consists of tensile strain failure, axial splitting tensile failure, and crushing failure [25]. Li et al. performed the numerical study on the failure of sandstone, limestone, and dolomite under impact loading [26]. The failure modes of rock are integrity, cleavage, and smashing.

Although many studies on mechanical properties of rock under impact loadings have been conducted [27–40], little attention was paid to the dynamic behavior of mudstone in coal mine. In consequence, this study is aimed at investigating the dynamic mechanical properties of mudstone in coal mine using the energy characterization method, and their quantitative relation formula was also developed. In the present study, a series of compression experiments of mudstone under different impact loadings from Huainan mining area, China, was conducted to study the mudstone dynamic behaviors, crack properties, and energy dissipation law using the diameter 50 mm SHPB test device. The relationships of crack and material composition of mudstone were determined. From the perspective of energy absorption, the deformation, failure, and energy dissipation of mudstone were described. The study provides good theoretical and technical supports for coal-rock roadway blasting excavation construction.

2. Theoretical Basis of SHPB Tests

In the conventional SHPB technique, the mudstone specimen is located in between the incident bar and the transmitted bar. The SHPB device is shown in Figure 1. When the striker bar hits the incident bar, a rectangular stress pulse is generated and travels along the incident bar until it strikes the specimen. Parts of the incident stress pulse reflect from the bar/specimen interface because of the material impedance mismatch. And part of it transmits through the specimen. The transmitted pulse emitted from the specimen travels along the transmitted bar until it strikes the end of the bar. The SHPB device is from Anhui University of Science and Technology. The length of the striker, incident bar, and transmitted bar is 0.60 m, 2.40 m, and 1.20 m, respectively. All the material of the bar is alloy steel. And the density of the bar is 7.8 g/cm^3, Young's modulus is 210 GPa, and longitudinal wave velocity is 5.19 km/s, respectively.

Under the failure of rock subjected to impact loading, rock constantly exchanges energy with the exotic environment. It is an evolutionary process that the microcracks vary from disorder to order and finally develop into macrocracks. The process from microdamage to macrofracture is the process of energy dissipation [41]. Hence, the failure mechanism can be easily revealed by energy analysis. In SHPB tests, both the stress and strain can be obtained in terms of the recorded strains of the incident and transmitted bars. During the impact loading, the incident energy $W_I(t)$, transmitted energy $W_R(t)$, and reflected energy $W_T(t)$ of specimens are as follows [12, 22, 32]:

$$W_I(t) = AEC_0 \int_0^t \varepsilon_I^2(t) dt, \tag{1}$$

$$W_R(t) = AEC_0 \int_0^t \varepsilon_R^2(t) dt, \tag{2}$$

$$W_T(t) = AEC_0 \int_0^t \varepsilon_T^2(t) dt, \tag{3}$$

where A is the section area of the bar, E is Young's modulus of the bar, and C_0 is the wave velocity of the bar. $\varepsilon_I(t)$, $\varepsilon_R(t)$, and $\varepsilon_T(t)$ are the strain of the incident wave, reflected wave, and transmitted wave at time t, respectively.

By omitting the wasted energy induced by the friction force between the specimen and incident bar, transmitted bar during the impact loadings, the absorbed energy of specimen $W_S(t)$ is

$$W_S(t) = W_I(t) - [W_R(t) + W_T(t)]. \tag{4}$$

3. Specimen Preparation and Physics

3.1. Preparation of Specimens.
Located in the central of Anhui province, China, middle and lower reaches of Yangtze River (see in Figure 2), the Panyi mine is faced with the danger of high in situ stress, water pressure, and temperature in rock roadway construction. This mining area was in use in
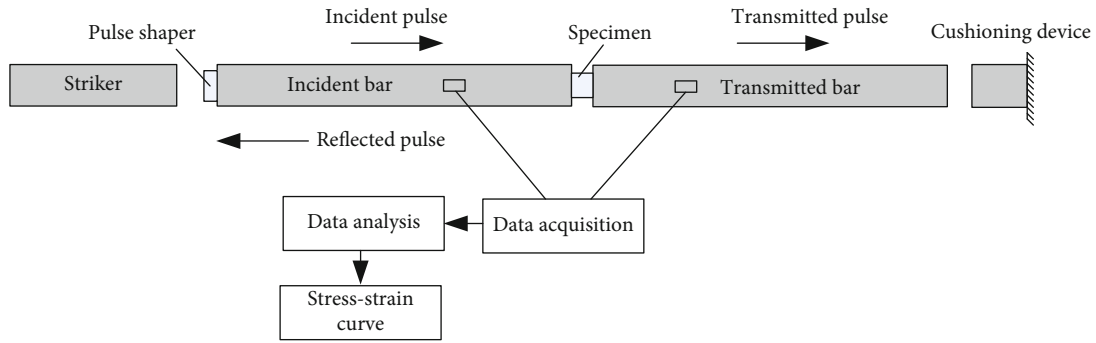
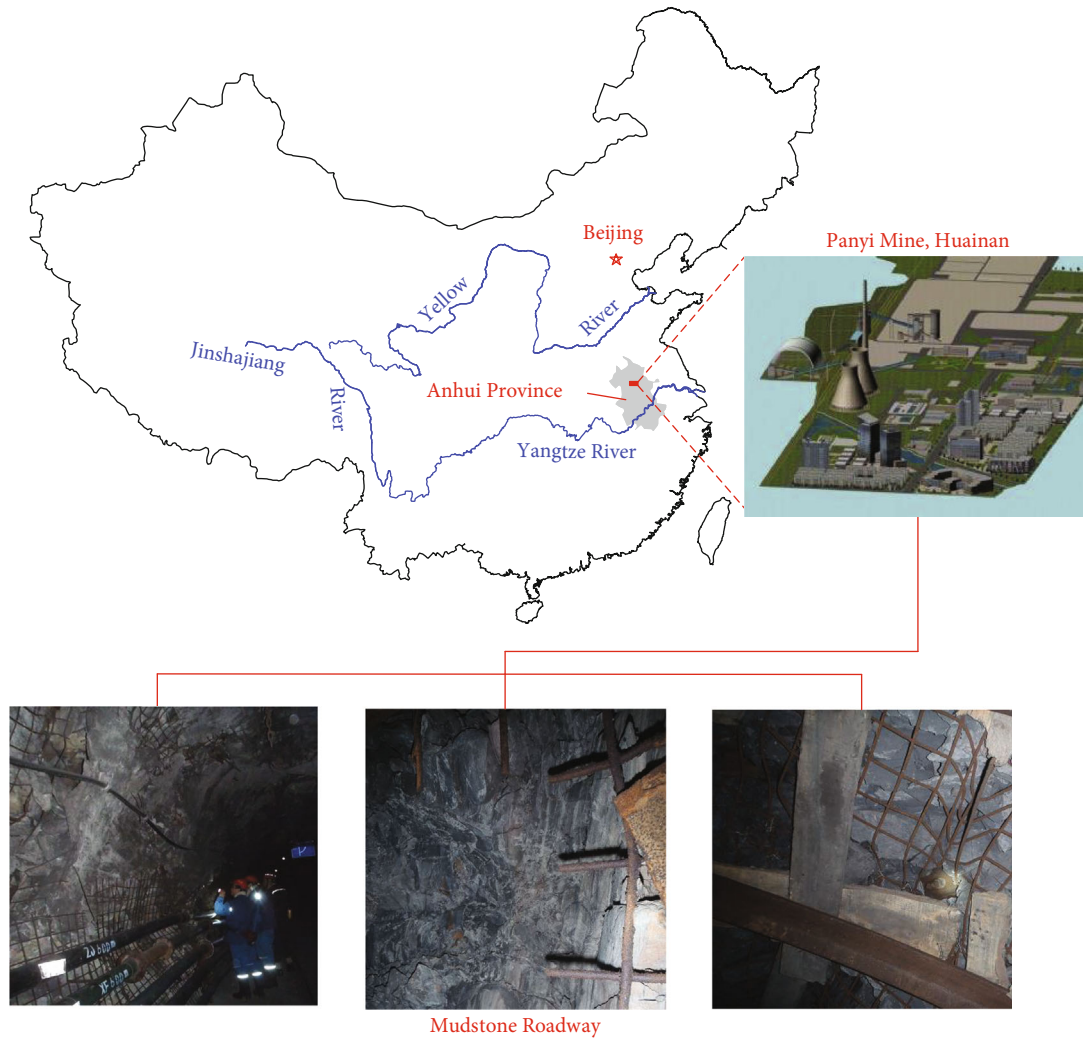FIGURE 1: Structural constituents of SHPB device.

FIGURE 2: Specimen location: Panyi mining area, Huainan, China.

December 2016. The roadway floor heave and side extrusion deformation were found in 2017. The mudstone blocks, used to be in experiments, originated from the 800 m deep 5# coal seam mining area as shown in the geological section in Figure 3. The coal mine area consists of mudstone, sandstone, and coal formations dipping about 40° to the south in the area of interest. There are some faults passing through the mudstone-sand layers, easily leading to rock fall. The mudstone forms in the development period of continental strong tensional faulting and experienced main squeezing and luffing tectonic and hydrothermal alteration activity.

The cylindrical specimens are obtained by drilling, cutting, and grinding in the laboratory. In order to meet the assumption of one-dimensional stress wave propagation
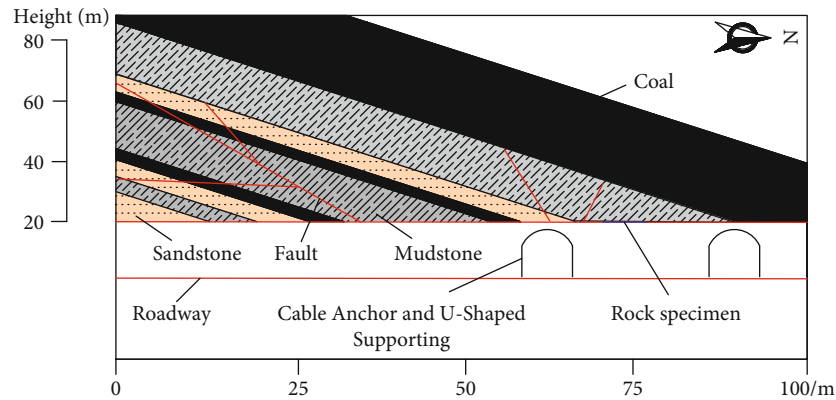
FIGURE 3: Geological section along 5# coal seam mining area. The obtained rock specimen is located within mudstone that dips approximately 40 deg south.
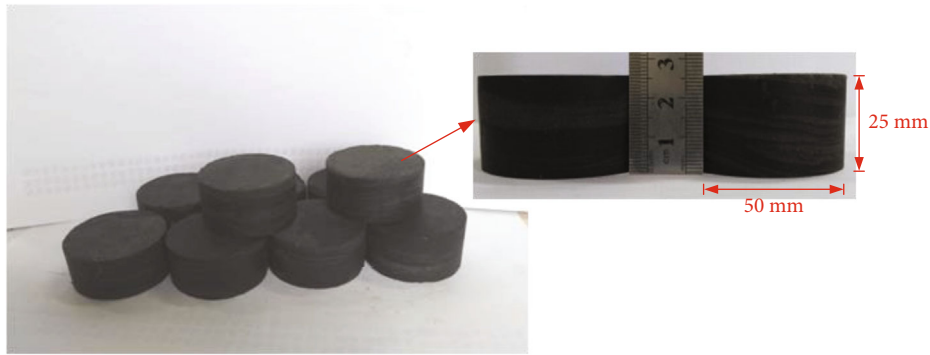

FIGURE 4: Mudstone specimen: diameter 50 mm and length 25 mm.

theory of SHPB and reduce the friction and axial inertia effect of the specimen, the length-diameter ratio of the prepared specimens is 0.5. Hence, the diameter of the specimen is 50 mm; the length of the specimen is 25 mm. No parallelism is within 0.05 mm on both ends of the specimen, and the roughness is within 0.02 mm. Those mudstone specimens in coal mine are shown in Figure 4.

Before testing, the process of saturating specimens with liquid was conducted using the vacuum saturation device (ZYB-IA, see Figure 5), by following the below procedure. Distilled water was used as a saturated liquid to avoid the potential influence of chemical factors.

(1) Put the dry mudstone specimen in a basket in the vacuum saturation device

(2) Vacuum the specimen storehouse until no air bubbles were generated in the liquid storage tank

(3) Switch on the specific valve; the distilled water in the liquid storage tank was sucked into the specimen storehouse

(4) The mudstone specimen was immersed in the distilled water (i.e., vacuum water-saturated environment) for 7 days, and the saturation pressure was set as 1.0 MPa

FIGURE 5: Vacuum saturation device (ZYB-IA).

(5) Take out the mudstone specimen for the next step of testing

3.2. Physics and Mechanical Properties of Mudstone Specimen.
The chemical composition of mudstone has much effect on the macromechanical properties of mudstone specimens. The chemical composition of mudstone in coal mine was determined using X-ray fluorescence (XRF) and X-ray Diffraction (XRD) by grinding the mudstone specimen after

TABLE 1: The chemical composition of mudstone in coal mine.

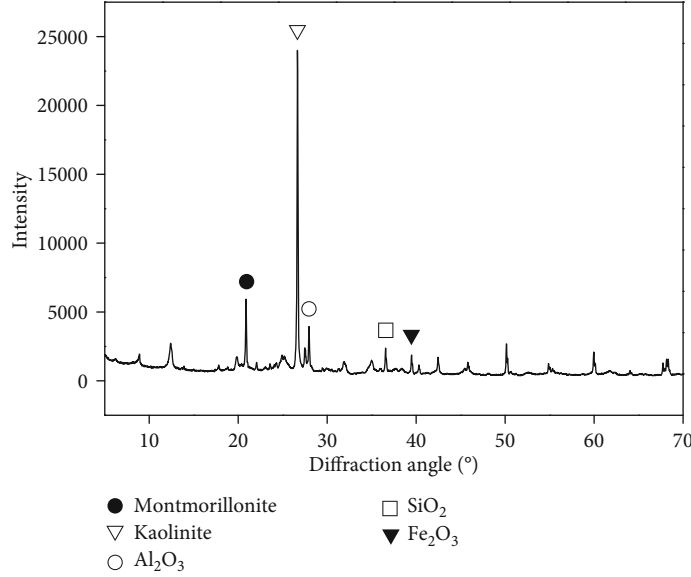| Chemical component	Na_2O	MgO	Al_2O_3	SiO_2	K_2O	TiO_2	Fe_2O_3	CaO
Percent (%)	1.200	1.943	20.383	56.616	3.989	1.419	12.328	0.964

FIGURE 6: The XRD spectra of mudstone.

drying. The results of XRF and XRD are plotted in Table 1 and Figure 6. It is shown that a total of 8 components are identified in mudstone. The main products are silicon dioxide (SiO_2), aluminum oxide (Al_2O_3), and iron trioxide (Fe_2O_3), reaching 56.6%, 20.38%, and 12.32%, respectively. And sodium oxide (Na_2O) is the least of the ingredients. In terms of mineral composition, kaolinite is one of the largest minerals in mudstone. Hence, the strength of mudstone is low, compared with other rocks. The static mechanical properties of mudstone were also tested, which results are shown in Table 2. The compressive strength and tensile strength of mudstone specimens are 28.96 MPa and 2.16 MPa, respectively. Hence, the strength of mudstone is lower than that of other rocks from coal mine.

4. The Procedure of Tests

Three kinds of drive pressure were applied to saturated mudstone specimens in the SHPB tests. The impact pressure is 0.25 MPa, 0.30 MPa, and 0.40 MPa, respectively, used in the SHPB tests. An approximate uniform deformation of the rock specimen is a prerequisite of the valid dynamic uniaxial compression tests. Before the tests, the dynamic stresses on both ends of the specimen should be roughly identical. This can be checked by comparing the stress histories on both ends of the specimen during the dynamic tests. Figure 7 illustrates the dynamic stress balance on both ends of the specimen for the typical test. It is clear that in this test, the uniformity of the dynamic stress across the specimen has been achieved, and thus, the axial inertial effect has been reduced to a negligible level, verifying that the SHPB test

TABLE 2: Static mechanical properties of mudstone.

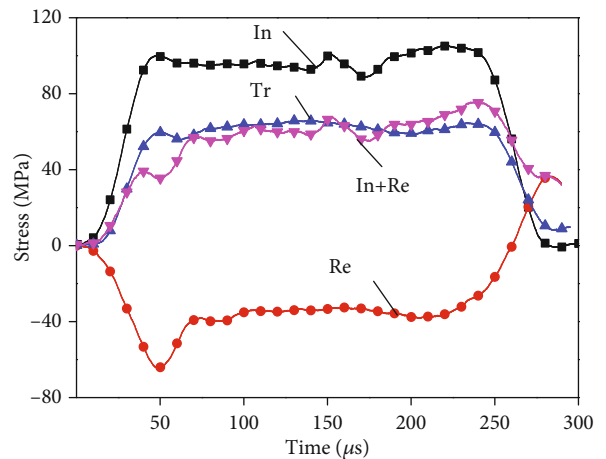| Density (g/cm^3)	Longitudinal wave velocity (m/s)	Compressive strength (MPa)	Tensile strength (MPa)	Poisson ratio
2.57	2176	28.96	2.16	0.23

FIGURE 7: Strain balance check for a typical dynamic SHPB test with pulse shaping. In: incident wave; Re: reflected wave; Tr: transmitted wave.

conforms to the assumption of one-dimensional stress wave. With the dynamic stress balance, the stress-strain curves of rocks can be obtained under different drive pressures in
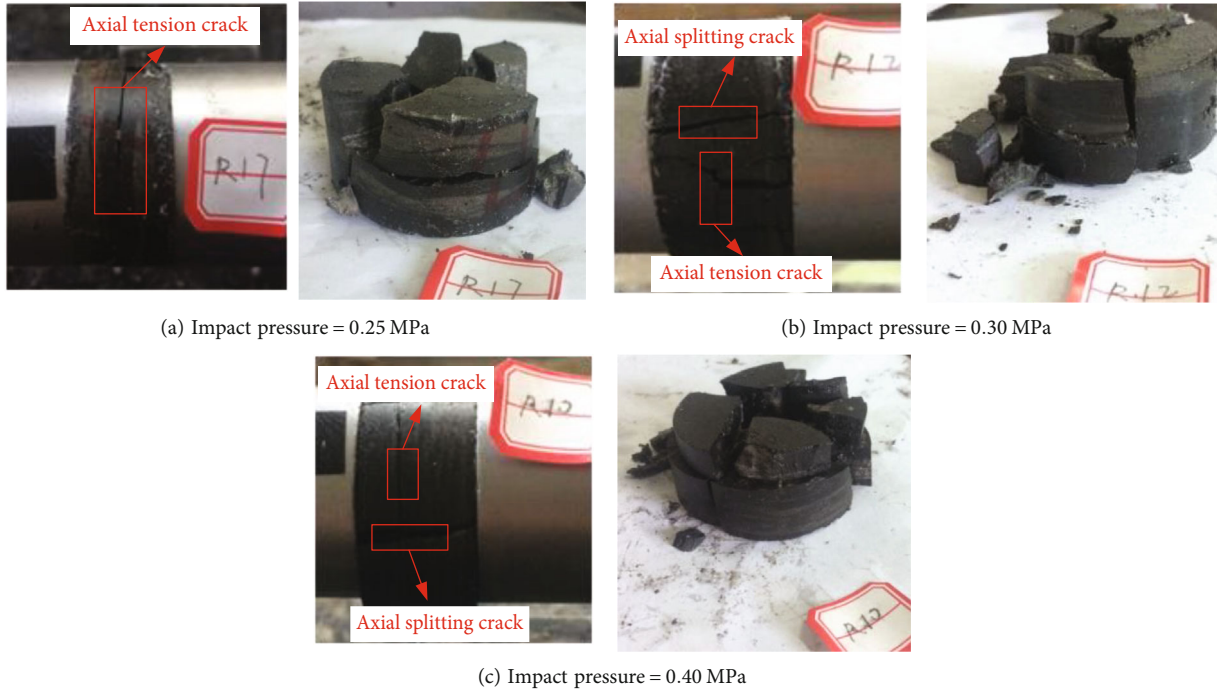
(a) Impact pressure = 0.25 MPa

(b) Impact pressure = 0.30 MPa

(c) Impact pressure = 0.40 MPa

FIGURE 8: Crack morphology of mudstone under different impact pressures.

5. Results of SHPB Tests

5.1. Failure Mode of SHPB Tests. Figure 8 shows the failure models of saturated mudstone under different impact loadings. It is shown that as the impact pressure increases, both the length and aperture of cracks in the mudstone specimen increase. A main circular crack appears in the mudstone specimen when impact pressure is 0.25 MPa. The crack passes throughout the whole specimen, and the length and aperture further increase. There are other cracks along the axial of specimens, which length is small. The specimen is broken into large blocks, due to the circular and axial cracks. When the impact pressure reaches 0.30 MPa, the number of axial cracks increases and some cracks extend to circular cracks of specimens, which is shown in Figure 8(b). At the same time, many split cracks are found in the test, and the size of these split cracks is large. Under the 0.40 MPa impact pressure, the cracks along with the axial of the specimen further extend and finally pass throughout the whole specimen. And the aperture of circular and axial cracks increases. The specimen is broken into lots of smaller blocks.

5.2. Dynamic Stress-Strain Curve. The stress-strain curves of mudstone specimens under different impact loadings are shown in Figure 9. The dynamic stress-strain curve can be divided into four stages: (I) elastic stage, (II) crack expansion stage, (III) plastic deformation stage, and (IV) failure stage, seen in Figure 10. In the elastic stage, stress increases linearly with strain increasing. When reaching elastic limit stress, the microcrack will generate and expand. The plastic deforma-

tion stage will appear under the larger strain. In addition, the dynamic strength increases slowly in this stage. After yield stress, the stress dramatically decreases with an increase of strain. The specimen is finally destroyed. The failure model can be seen in Figure 8. Unlike the general relationships of stress and strain, there is no existence of the initial crack closure stage. The main reason is the fact that the high strain ratio leads the internal microcracks not to be closed in time and directly enter the elastic stage. It can be also inferred in Figure 9 that as the impact loading increases, the dynamic strength of the mudstone specimen increases.

5.3. Time-History Curve of Energy under Impact Loading. According to Equations (1), (2), (3), and (4), the incident energy, absorbed energy, transmitted energy, and reflected energy at any time can be obtained. The results are shown in Figure 11. It is illustrated that all the energy increases with an increase in time. The incident energy grows fastest. In addition, the intensity of incident energy is largest, the transmitted energy is second, and the reflected energy is smallest. The incident energy, absorbed energy, transmitted energy, and reflected energy at the final time are 103 J, 44.3 J, 42.2 J, and 16.5 J, respectively.

Combined with the crack morphology of the mudstone specimen shown in Figure 8, the energy absorption process of the mudstone specimen can be divided into three stages from the perspective of absorbed energy.

(1) *First Stage.* The absorbed energy increases during 0 to 50 μs. The mudstone specimen is at the elastic compressive deformation condition. The absorbed energy exists in the form of elastic energy.

(a) Impact pressure = 0.25 MPa

(b) Impact pressure = 0.30 MPa
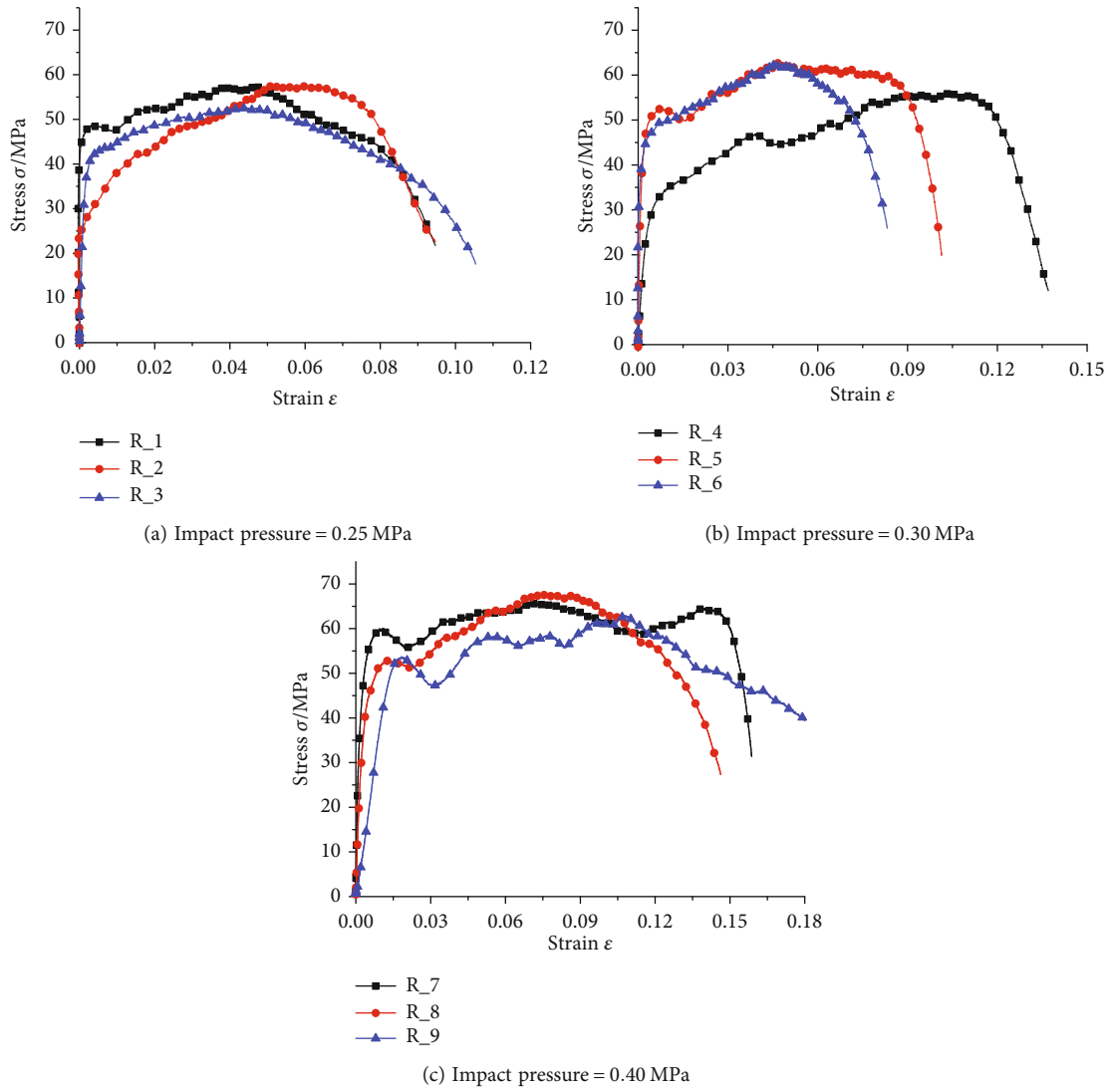
(c) Impact pressure = 0.40 MPa

FIGURE 9: Dynamic stress-strain curves of mudstone specimens under different impact loadings.
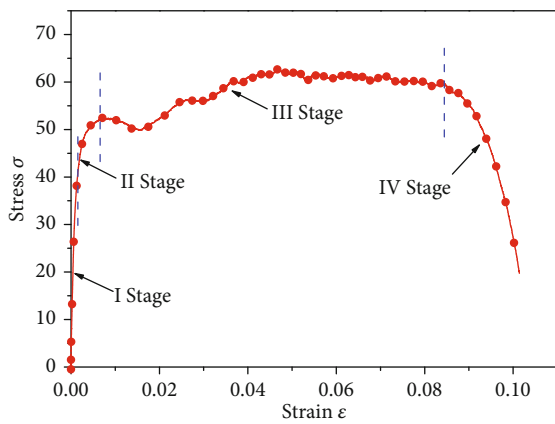

FIGURE 10: The typical stress-strain curve of mudstone under impact loading.
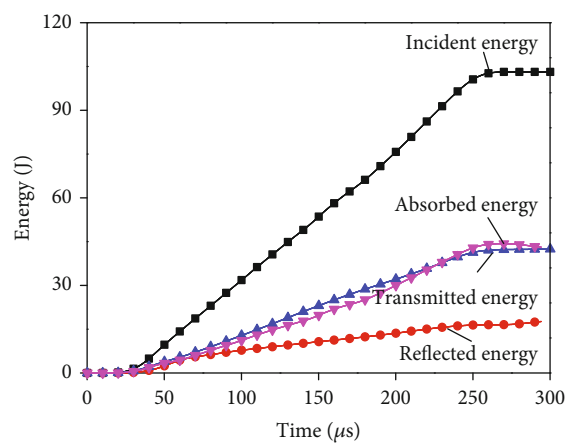
FIGURE 11: The time-history curve of energy under impact loading.

TABLE 3: Results of energy dissipation of mudstone under different impact loadings.

| Number	Drive pressure (MPa)	Scale Diameter (mm)	Length (mm)	Impedance (10^5 g/(cm^2 s))	Incident energy (J)	Transmitted energy (J)	Reflected energy (J)	Absorbed energy (J)	Energy dissipation density (J·cm^{-3})	Average strain ratio (s^{-1})	Dynamic compressive strength (MPa)	Peak strain
1	0.25	49.83	26.19	4.91	54.94	28.14	7.64	19.16	0.375	45	57.50	0.0099
2	0.25	49.95	26.11	5.59	52.53	26.19	12.93	13.44	0.262	47	56.65	0.0111
3	0.25	50.05	24.08	5.76	50.53	23.17	7.77	19.59	0.414	42	52.50	0.0117
4	0.3	49.64	25.56	4.40	60.37	30.01	9.88	20.48	0.414	53	55.32	0.0138
5	0.3	50.05	25.30	4.55	68.19	36.70	7.96	23.53	0.473	62	62.30	0.0103
6	0.3	49.88	26.76	5.16	61.80	33.7	7.10	21.00	0.404	60	62.13	0.0098
7	0.4	50.04	26.06	5.49	103.15	42.43	17.64	43.09	0.841	71	64.34	0.015
8	0.4	49.97	26.65	4.29	96.35	38.57	14.50	43.24	0.828	66	67.69	0.016
9	0.4	49.74	25.78	5.30	105.51	40.20	16.59	48.72	0.973	70	63.57	0.0212

(a)

(b)

(c)
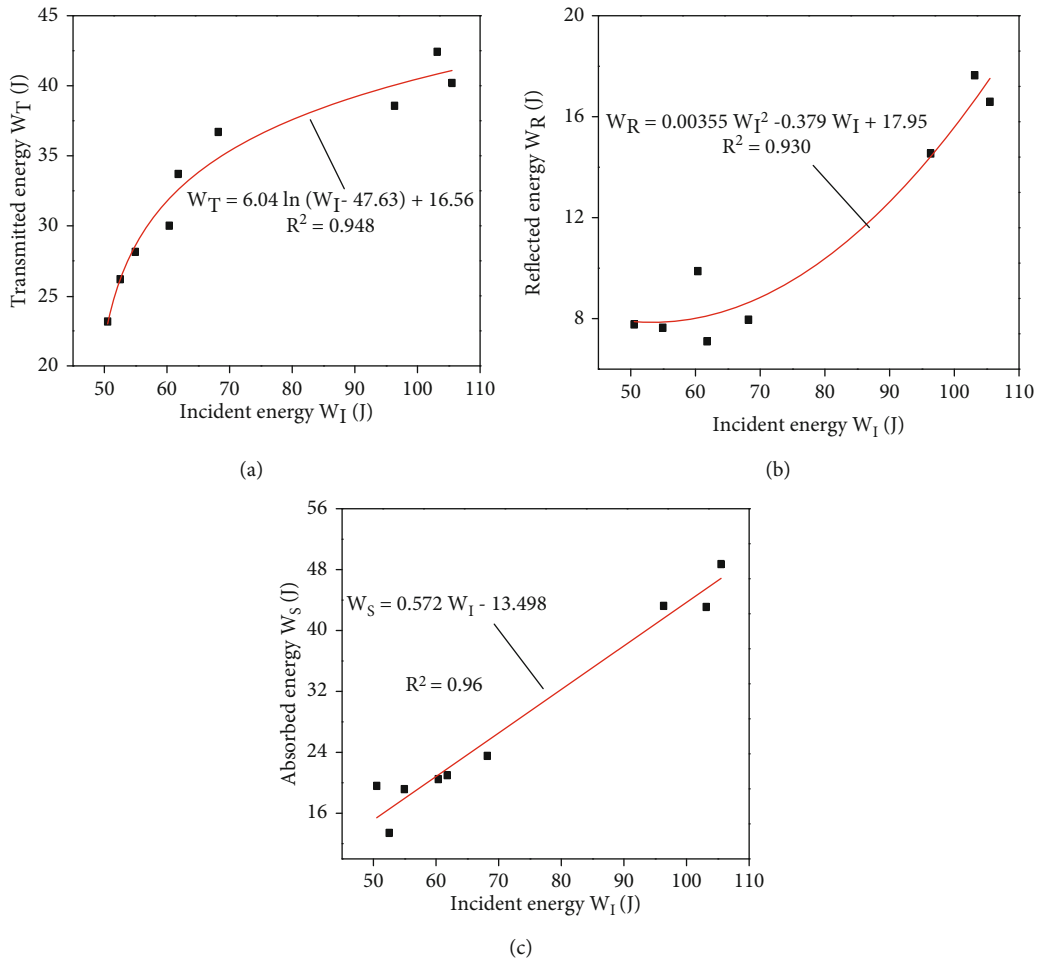
FIGURE 12: The relationships between incident energy and transmitted energy, reflected energy, and absorbed energy.
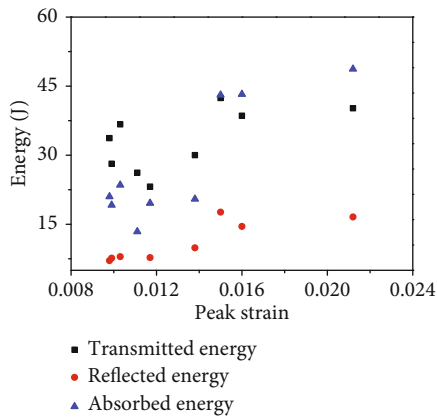

FIGURE 13: The relationship between energy and peak strain of mudstone specimens.

(2) *Second Stage.* This stage begins at 50 to 200 μs. The absorbed energy of the specimen is smaller than reflected energy in the earlier stage and then is larger than reflected energy after 80 μs. The main reason can be summarized as follows. The incident end sur-

face of the specimen would generate reflected tensile stress and transfer reflected energy under incident stress waves, due to a mismatch between the wave impedance of the specimen and the bar. In this state, the absorbed energy is smaller than reflected energy. However, the contact surface will be smooth and the reflected energy will decrease under the incident bar continuously impacting. The circular crack will generate under the tensile stress wave. Subsequently, under the effect of high incident stress, the original microcracks inside the mudstone specimen extend, and a large number of new microcracks are generated at the same time, and the absorption energy continues to increase slowly.

(3) *Third Stage.* After 200 μs, the primary cracks in the mudstone specimen rapidly expand and new cracks will generate and pass through the specimen. And then, the axial cracks will be produced. Because there is no energy supplement, eventually, the energy tends to have a stable energy value.

5.4. The Relationships of Incident Energy and Transmitted Energy and Reflected Energy. The final incident energy,
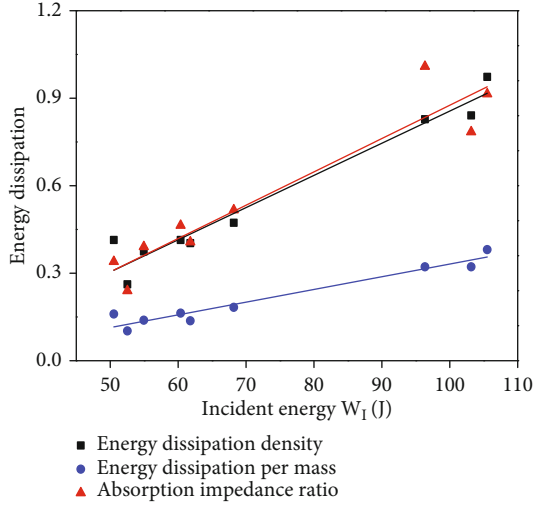
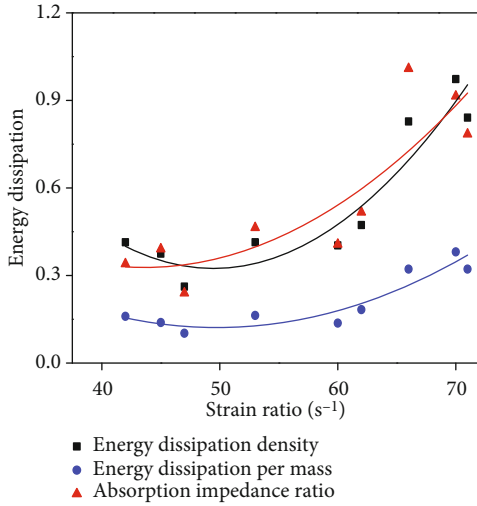FIGURE 14: The relationship between energy indexes and incident energy.

FIGURE 15: The relationship between energy indexes and average strain rate.

absorbed energy, transmitted energy, and reflected energy time can be obtained using Equations (1), (2), (3), and (4). The relationships of all the energy are shown in Table 3 and Figure 12.

It is indicated from Figure 12(a) that when the incident energy is smaller, the transmission energy increases with the increase of the incident energy. When the incident energy is larger, the transmission energy increment decreases with the increase of the incident energy. For the lower incidence energy, the mudstone specimen is in the elastic stage. With the increase of the incident energy, the mudstone is in the plastic stage, the inner primary microcrack growth and the new microcrack are produced, and the transmission of the transmission wave is weakened.

As shown in Figure 12(b), when the incident energy is small, the reflected energy increases slowly with the increase of the incident energy. When the incident energy

exceeds 70 J, the reflected energy increases faster; the transmission energy tends to be stable. It is known from Figure 12(c) that the absorbed energy of the specimen increases linearly with the increase of the incident energy, and the absorbed energy is less than 0.5 times the incident energy. It is indicated that more than half of the energy of the impact incident can be dissipated in the form of an elastic wave of the bars.

5.5. The Relationships of Absorbed Energy, Transmitted Energy, and Reflected Energy between Peak Strains. The energy transmission is related to the deformation of mudstone specimens. Hence, the relationships of absorbed energy, transmitted energy, and reflected energy between peak strains are plotted in Figure 13. It is shown that as the peak strain increases, the absorbed energy, transmitted energy, and reflected energy increase. However, the increases are different among the absorbed energy, transmitted energy, and reflected energy, and there is some volatility during the increases. And the largest growth in energy is absorbed energy. The reason is that the deformation increments of mudstone specimens need more energy.

5.6. EDV, EDM, and AIER. Three energy dissipation indexes were introduced to represent the energy absorption characteristics of mudstone specimens. One is absorbed energy per volume (EDV) w_d, which is defined as follows:

$$w_d = \frac{W_s}{V_s},\tag{5}$$

where V_s is the volume of rock specimens. Considering the effect of mass, the second index is defined as absorbed energy per mass (EDM) m_d. The formula is

$$m_d = \frac{W_s}{M_s},\tag{6}$$

where M_s is the volume of rock specimens. The impedance of mudstone specimens is closely related to the energy transfer efficiency. Hence, introducing the impedance, the third index is defined as

$$Z_w = \frac{W_s}{\rho C_s},\tag{7}$$

where Z_w is absorption impedance energy ratio (AIER).

The relationships between three indexes and incident energy are plotted in Figure 14. Also plotted in Figure 14 are the best-fitted curves for the data using the linear function, implying that the linear relationship between the three indexes and incident energy fits the flow data very well for most of the data points. Comparing with the fitting coefficient (R^2) of three indexes (w_d, m_d, Z_w), the best fitting is the relationship of AIER and incident energy, and this fitting coefficient is 0.936. It is indicated that AIER Z_w, which takes into account the wave impedance property, can more effectively reflect the energy

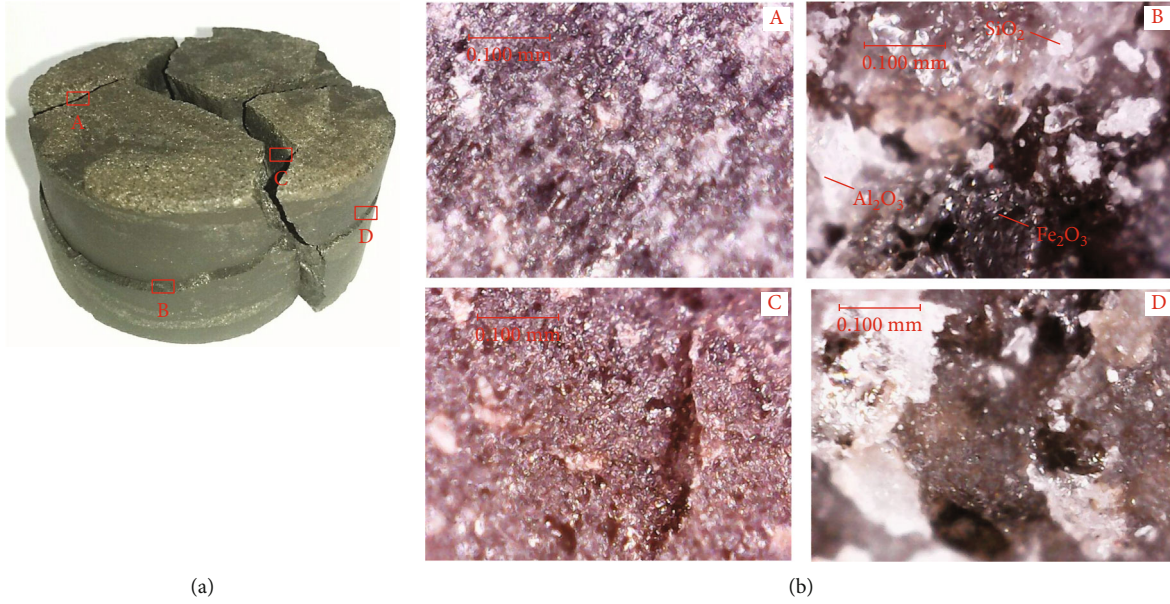(a)   (b)

Figure 16: The crack characteristic of mudstone under impact loading: (a) axial splitting and axial tension crack locations numbered as A, B, C, and D, respectively; (b) crack micrograph under electron digital microscope ($\times 1000$).

absorption of mudstone specimens:

$$w_d = 0.011W_I - 0.247 \ (R^2 = 0.848),$$
$$m_d = 0.004W_I - 0.104 \ (R^2 = 0.836), \quad (8)$$
$$Z_w = 0.114W_I - 0.267 \ (R^2 = 0.936).$$

5.7. The Effect of Energy Dissipation on Strain Ratio. The relationships between EDV, EDM, and AIER and average strain ratio ε are plotted in Figure 15. The quadratic function can be used to describe the relationships between three indexes and average strain ratio. When the strain rate is low, the absorbed energy causes mudstone with many internal defects. When the strain rate increases, the increase of the absorbed energy of the specimen will cause the new microcracks to generate in the mudstone specimens. When the strain rate is high, the original microcracks in the mudstone expand and pass through the mudstone specimens. And the specimen is crushed and broken finally:

$$w_d = 0.0041\dot{\varepsilon}^2 - 0.134\dot{\varepsilon} + 3.65 \ (R^2 = 0.855),$$
$$m_d = 0.0005\dot{\varepsilon}^2 - 0.055\dot{\varepsilon} + 1.49 \ (R^2 = 0.827), \quad (9)$$
$$Z_d = 0.0008\dot{\varepsilon}^2 - 0.069\dot{\varepsilon} + 1.85 \ (R^2 = 0.678).$$

6. Discussion

In order to understand the fact that chemical components and microstructures lead to the macrocrack phenomenon of saturated mudstone specimens under impact loading, the crack morphology was observed using the BIST digital microscope. Two axial and two circular crack surfaces of the typical broken mudstone specimen were selected to examine and numbered A, B, C, and D. Obvious roughness characteristics are easily observed in two kinds of crack surfaces, shown in Figure 16. But the roughness of the circular surface is greater than that of the axial surface. The main reason is that the axial crack surface (A and C) is caused by shear slip and wearing, and the stress wave tension results in the circular crack surface (B and D) under impact loadings. In addition, from Table 1, SiO_2 is one of the main components in mudstone, followed by Al_2O_3 and Fe_2O_3. Their grain distribution is shown in Figure 8(b). And it is concluded that both the axial and circular cracks mainly occur in the grain interface, because it is a weak area in rock.

Combining the one-dimensional stress wave propagation theory and physics component of mudstone, the reason for the generation of circular and axial cracks in specimens under impact loadings is as follows. Mudstone is characterized by viscoplasticity, softening, and low structural strength. The microstructure of mudstone will change when suffering from impact loading. The microparticle of mudstone is redistributed along with forced direction from the free condition. In the SHPB test, the incident stress reflects and transmits to tensile stress when the stress transmits to the contact surface between transmitted bar and specimen. The tensile stress causes the circular crack due to the low tensile strength of the mudstone in the coal mine specimen. Meanwhile, under the continuous action of the incident compression stress wave, the specimen is subjected to axial splitting failure.

Drill-blasting is the main way for roadway tunneling in coal mine. Generally, the cylindrical charge is used for blasting holes, and the surrounding rock is in a one-dimensional compression situation. In addition, the effect of blasting energy on blasting fragmentation and damage of reserved rock is important for drill-blasting, especially for mudstone

with low strength. Hence, the energy dissipation law and failure mechanism of mudstone under impact loading provide strong support for mining blasting safety.

7. Conclusions

In this paper, the dynamic mechanical properties of mudstone in coal mine are investigated using the energy characterization method, and their quantitative relation formula is also developed. Therefore, a series of compression experiments of mudstone under different impact loadings are conducted to study the mudstone dynamic behaviors, crack properties, and energy dissipation law using the diameter 50 mm SHPB test device. The above analyses support the following conclusions:

(1) The axial splitting failure and circular tensile failure are observed in mudstone specimens during the test. It is because the tensile stress would be generated and easily cause circular tensile failure for low strength rock due to the reflection and transmission effect of the transmitted bar. Additionally, continuous compressive stress leads to axial splitting failure

(2) It is shown from the crack micromorphology that the failure surface appears in the mudstone grain interface, and the roughness of the tensile failure surface is greater than that of the splitting surface

(3) The absorbed energy, transmitted energy, and reflected energy of mudstone increase with the increase of incident energy, showing linear, logarithmic, and quadratic functions, respectively

(4) Comparing the three energy dissipation indexes (EDV, EDM, and AIER) with incident energy, the AIER is more a reflection of the energy dissipation of mudstone. The quadratic function relationship between three energy dissipation indexes and average strain rate of mudstone specimen shows a strong dependence of strain rate

Data Availability

The datasets used or analyzed during the current study are available from the corresponding author on reasonable request.

Conflicts of Interest

The authors declare no conflicts of interest.

Authors' Contributions

Both Liangjie Guo and Yongyu Wang proposed the research. Liangjie Guo contributed to the SHPB tests and writing the manuscript; Yongyu Wang contributed to the specimen preparation and revision of the manuscript.

References

[1] F. R. Ma and P. L. Li, "Experiment analysis on the mechanical properties of the horizontally stratified mudstone," *Advanced Materials Research*, vol. 1065-1069, pp. 31–34, 2014.

[2] L. Zhang, X. Mao, and R. Liu, "The impact of loading rate on mechanical property of mudstone at high temperatures," *Electronic Journal of Geotechnical Engineering*, vol. 19, pp. 3019–3027, 2014.

[3] A. G. Corkum and C. D. Martin, "The mechanical behaviour of weak mudstone (Opalinus clay) at low stresses," *International Journal of Rock Mechanics and Mining Sciences*, vol. 44, no. 2, pp. 196–209, 2007.

[4] A. Taheri and K. Tani, "Use of down-hole triaxial apparatus to estimate the mechanical properties of heterogeneous mudstone," *International Journal of Rock Mechanics and Mining Sciences*, vol. 45, no. 8, pp. 1390–1402, 2008.

[5] L. A. N. R. Douma, M. I. W. Primarini, M. E. Houben, and A. Barnhoorn, "The validity of generic trends on multiple scales in rock-physical and rock- mechanical properties of the Whitby Mudstone, United Kingdom," *Marine and Petroleum Geology*, vol. 84, pp. 135–147, 2017.

[6] X. L. Lei, O. Nishizawa, K. Kusunose, A. Cho, T. Satoh, and O. Nishizawa, "Compressive failure of mudstone samples containing quartz veins using rapid AE monitoring: the role of asperities," *Tectonophysics*, vol. 328, no. 3–4, pp. 329–340, 2000.

[7] J. Luo and L. Wang, "High-temperature mechanical properties of mudstone in the process of underground coal gasification," *Rock Mechanics and Rock Engineering*, vol. 44, no. 6, pp. 749–754, 2011.

[8] P. Bhattarai, H. Marui, B. Tiwari, N. Watanabe, G. R. Tuladhar, and K. Aoyama, "Influence of weathering on physical and mechanical properties of mudstone," *Physical Review B*, vol. 80, no. 23, pp. 308–310, 2006.

[9] X. Huang, J. Liu, C. Yang, and J. W. Chen, "Experimental investigation of Daqing Oilfield mudstone's creep characteristic under different water contents," *Journal Central University of Technology*, vol. 15, no. s1, pp. 471–474, 2008.

[10] L. Zhang, X. Mao, R. Liu, X. Guo, and D. Ma, "The mechanical properties of mudstone at high temperatures: an experimental study," *Rock Mechanics and Rock Engineering*, vol. 47, no. 4, pp. 1479–1484, 2014.

[11] Y. Lu, L. Wang, X. Sun, and J. Wang, "Experimental study of the influence of water and temperature on the mechanical behavior of mudstone and sandstone," *Bulletin of Engineering Geology and the Environment*, vol. 76, no. 2, pp. 1–16, 2016.

[12] Z. Zhou, X. Li, Z. Ye, and K. Liu, "Obtaining constitutive relationship for rate-dependent rock in SHPB tests," *Rock Mechanics and Rock Engineering*, vol. 43, no. 6, pp. 697–706, 2010.

[13] F. Dai, S. Huang, K. Xia, and Z. Tan, "Some fundamental issues in dynamic compression and tension tests of rocks using split Hopkinson pressure bar," *Rock Mechanics and Rock Engineering*, vol. 43, no. 6, pp. 657–666, 2010.

[14] C. Zou and L. N. Y. Wong, "Size and geometry effects on the mechanical properties of Carrara marble under dynamic loadings," *Rock Mechanics and Rock Engineering*, vol. 49, no. 5, pp. 1695–1708, 2016.

[15] Y. Chen, A. Lu, X. Mao, M. Li, and L. Zhang, "Nonlinear dynamics mechanism of rock burst induced by the instability of the layer-crack plate structure in the coal wall in deep coal mining," *Shock and Vibration*, vol. 2017, no. 10, Article ID 4051967, 2017.

[16] S. Demirdag, K. Tufekci, R. Kayacan, H. Yavuz, and R. Altindag, "Dynamic mechanical behavior of some carbonate rocks," *International Journal of Rock Mechanics and Mining Sciences*, vol. 47, no. 2, pp. 307–312, 2010.

[17] Y. Hao and H. Hao, "Numerical investigation of the dynamic compressive behaviour of rock materials at high strain rate," *Rock Mechanics and Rock Engineering*, vol. 46, no. 2, pp. 373–388, 2013.

[18] R. Shan, Y. Jiang, and B. Li, "Obtaining dynamic complete stress-strain curves for rock using the split Hopkinson pressure bar technique," *International Journal of Rock Mechanics and Mining Sciences*, vol. 37, no. 6, pp. 983–992, 2000.

[19] Z. M. Chen, Y. X. Li, and Z. Zhang, "Experimental study of dynamic mechanical properties of granite," *Applied Mechanics and Materials*, vol. 858, pp. 86–90, 2016.

[20] J. Z. Liu, J. Y. Xu, X. C. Lv, D. H. Zhao, and B. L. Leng, "Experimental study on dynamic mechanical properties of amphibolites, sericite-quartz schist and sandstone under impact loadings," *International Journal of Nonlinear Sciences and Numerical Simulation*, vol. 13, no. 2, pp. 209–217, 2012.

[21] A. Mardoukhi, Y. Mardoukhi, M. Hokka, and V. T. Kuokkala, "Effects of heat shock on the dynamic tensile behavior of granitic rocks," *Rock Mechanics and Rock Engineering*, vol. 50, no. 5, pp. 1171–1182, 2017.

[22] D. F. Du HB, Y. Xu, Y. Liu, and H. N. Xu, "Numerical investigation on the dynamic strength and failure behavior of rocks under hydrostatic confinement in SHPB testing," *International Journal of Rock Mechanics and Mining Sciences*, vol. 108, pp. 43–57, 2018.

[23] L. F. Fan, Z. J. Wu, Z. Wan, and J. W. Gao, "Experimental investigation of thermal effects on dynamic behavior of granite," *Applied Thermal Engineering*, vol. 125, pp. 94–103, 2017.

[24] X. Li, F. Gong, J. Zhao, K. Gao, and T. Yin, "Test study of impact failure of rock subjected to one-dimensional coupled static and dynamic loads," *Chinese Journal of Rock Mechanics and Engineering*, vol. 29, no. 2, pp. 251–260, 2010.

[25] G. M. Zhao, W. W. Ma, and X. R. Meng, "Damage models and energy characteristics of rock-like materials under dynamic load," *Rock and Soil Mechanics*, vol. 36, no. 12, pp. 3598–3605, 2015.

[26] X. Li, H. Li, K. Liu et al., "Dynamic properties and fracture characteristics of rocks subject to impact loading," *Chinese Journal of Rock Mechanics and Engineering*, vol. 36, no. 10, pp. 2393–2405, 2017.

[27] C. Li, Y. Xu, P. Chen, H. Li, and P. Lou, "Dynamic mechanical properties and fragment fractal characteristics of fractured coal–rock-like combined bodies in split Hopkinson pressure bar tests," *Natural Resources Research*, vol. 29, no. 5, pp. 3179–3195, 2020.

[28] T. Chakraborty, S. Mishra, J. Loukus, B. Halonen, and B. Bekkala, "Characterization of three Himalayan rocks using a split Hopkinson pressure bar," *International Journal of Rock Mechanics and Mining Sciences*, vol. 85, pp. 112–118, 2016.

[29] Z. Yan, F. Dai, Y. Liu, A. Li, and H. du, "Numerical assessment of the rate-dependent cracking behaviours of single- flawed rocks in split Hopkinson pressure bar tests," *Engineering Fracture Mechanics*, vol. 247, p. 107656, 2021.

[30] H. Wu, B. Dai, L. Cheng, R. Lu, G. Zhao, and W. Liang, "Experimental study of dynamic mechanical response and energy dissipation of rock having a circular opening under impact loading," *Mining, Metallurgy & Exploration*, vol. 38, no. 2, pp. 1111–1124, 2021.

[31] Y. Luo, G. Wang, X. Li et al., "Analysis of energy dissipation and crack evolution law of sandstone under impact load," *International Journal of Rock Mechanics and Mining Sciences*, vol. 132, article 104359, 2020.

[32] C. Zhu, M. C. He, X. H. Zhang, Z. G. Tao, Q. Yin, and L. F. Li, "Nonlinear mechanical model of constant resistance and large deformation bolt and influence parameters analysis of constant resistance behavior," *Rock and Soil Mechanics*, vol. 42, no. 7, pp. 1911–1924, 2021.

[33] C. Zhu, M. C. He, B. Jiang, X. Z. Qin, Q. Yin, and Y. Zhou, "Numerical investigation on the fatigue failure characteristics of water-bearing sandstone under cyclic loading," *Journal of Mountain Science*, vol. 18, no. 12, pp. 3348–3365, 2021.

[34] G. Li, Y. Hu, and T. Sm, "Analysis of deformation control mechanism of prestressed anchor on jointed soft rock in large cross-section tunnel," *Bulletin of Engineering Geology and the Environment*, vol. 80, no. 12, pp. 9089–9103, 2021.

[35] M. Z. Gao, J. Xie, Y. N. Gao et al., "Mechanical behavior of coal under different mining rates: a case study from laboratory experiments to field testing," *International Journal of Mining Science and Technology*, vol. 31, no. 5, pp. 825–841, 2021.

[36] M. Z. Gao, H. C. Hao, S. N. Xue et al., "Discing behavior and mechanism of cores extracted from Songke-2 well at depths below 4,500 m," *International Journal of Rock Mechanics and Mining Sciences*, vol. 149, article 104976, 2022.

[37] C. Cao, W. Zhang, J. Chen, B. Shan, S. Song, and J. Zhan, "Quantitative estimation of debris flow source materials by integrating multi- source data: a case study," *Engineering Geology*, vol. 291, article 106222, 2021.

[38] Z. Dou, S. X. Tang, X. Y. Zhang et al., "Influence of shear displacement on fluid flow and solute transport in a 3D rough fracture," *Lithosphere*, vol. 2021, no. Special 4, 2021.

[39] F. Xiong, Q. Jiang, and C. Xu, "Fast equivalent micro-scale pipe network representation of rock fractures obtained by computed tomography for fluid flow simulations," *Rock Mechanics and Rock Engineering*, vol. 54, no. 2, pp. 937–953, 2021.

[40] F. Xiong, H. Sun, Z. Ye, and Q. Zhang, "Heat extraction analysis for nonlinear heat flow in fractured geothermal reservoirs," *Computers and Geotechnics*, vol. 144, p. 104641, 2022.

[41] B. Xie, X. Wang, and P. Lv, "Dynamic properties of bedding coal and rock and the SHPB testing for its impact damage," *Journal of Vibration and Shock*, vol. 36, no. 21, pp. 117–124, 2017.